



An investigation of the SO₂ content of the venusian mesosphere using SPICAV-UV in nadir mode

Emmanuel Marcq^{a,*}, Denis Belyaev^a, Franck Montmessin^a, Anna Fedorova^b, Jean-Loup Bertaux^a, Ann Carine Vandaele^c, Eddy Neefs^c

^aLATMOS, 11 Boulevard d'Alembert, F-78280 Guyancourt, France

^bSpace Research Institute (IKI), 117997, 84/32 Profsoyuznaya Str., Moscow, Russia

^cBelgian Institute for Space Aeronomy, Avenue Circulaire, 3, B-1180 Bruxelles, Belgium

ARTICLE INFO

Article history:

Received 19 February 2010

Revised 25 August 2010

Accepted 25 August 2010

Available online 8 September 2010

Keywords:

Venus, Atmosphere

Ultraviolet observations

Atmospheres, Composition

ABSTRACT

Using the SPICAV-UV spectrometer aboard *Venus Express* in nadir mode, we were able to derive spectral radiance factors in the middle atmosphere of Venus in the 170–320 nm range at a spectral resolution of $R \approx 200$ during 2006 and 2007 in the northern hemisphere. By comparison with a radiative transfer model of the upper atmosphere of Venus, we could derive column abundance above the visible cloud top for SO₂ using its spectral absorption bands near 280 and 220 nm. SO₂ column densities show large temporal and spatial variations on a horizontal scale of a few hundred kilometers. Typical SO₂ column densities at low latitudes (up to 50°N) were found between 5 and 50 μm-atm, whereas in the northern polar region SO₂ content was usually below 5 μm-atm. The observed latitudinal variations follow closely the cloud top altitude derived by SPICAV-IR and are thought to be of dynamical origin. Also, a sudden increase of SO₂ column density in the whole northern hemisphere has been observed in early 2007, possibly related to a convective episode advecting some deep SO₂ into the upper atmosphere.

© 2010 Elsevier Inc. All rights reserved.

1. Introduction

The clouds of Venus are made of small droplets of sulfuric acid concentrated at about 80%. In the visible, the albedo is very high, with about 85% of solar light being scattered back to space. On Earth, there is also a natural layer of such H₂SO₄ droplets around 20–25 km of altitude (the Junge layer), which is strongly re-enforced from episodic volcanic eruptions, through injection of SO₂ in the lower stratosphere as a first step to the production of H₂SO₄ droplets. The eruption of Mount Pinatubo (1991) was followed by a documented decrease of the averaged temperature of about 0.4 °C. It has been suggested (Crutzen, 2006) that the artificial injection of sulfur dioxide (SO₂) in the lower stratosphere could be one way to counterbalance Earth's global warming, in a so-called geo-engineering exercise. Therefore, there is a renewed interest for the study of Venus clouds, not only for Venus itself, but also in more general terms for potential applications to Earth.

Sulfur dioxide, a necessary precursor of H₂SO₄ droplets, was first identified in the upper atmosphere of Venus from ground based high resolution spectroscopy of Venus spectra in the range 299–340 nm (Barker, 1979). The same year, the stronger SO₂ band at 208–218 nm

was clearly identified with high resolution spectroscopy obtained with the telescope IUE (International Ultraviolet Explorer) by Conway et al. (1979). With the ultraviolet spectrometer UVS of Pioneer Venus, Stewart et al. (1979) identified also the presence of SO₂ in the UV reflectance (actually, ratio of reflectances at equator and polar regions) with two broad minima corresponding to the two UV bands of SO₂. Later, the presence of SO was detected also with IUE (Na et al., 1990), which bands are mixed with SO₂ bands in the region 200–220 nm. The most important and comprehensive previous Venus SO₂ data set is the one extracted from eight years of UV reflectance recorded in 1978–1986 with UVS/*Pioneer Venus* (Esposito et al., 1988). One important feature of their study is the very large variability of observed SO₂, ranging from ~0 to 70–100 ppbv (at 40 mbar), their Fig. 4. Comparison between Venera-15 IR data and Pioneer Venus data was also performed by Zasova et al. (1993). Another feature is the time decline of the SO₂ amount (averaged over periods of about a hundred days), rather fast over the first year, and much slower later on. This behavior was interpreted as a massive “injection of SO₂ into the Venus middle atmosphere by a volcanic explosion” (Esposito et al., 1988), as suggested earlier by Esposito (1984). Sulfur dioxide (SO₂) is also an abundant minor species in the lower atmosphere of Venus – 150 ppmv as reported by de Bergh et al. (2006) – and thus an enormous quantity of SO₂ is vertically convected up to levels where it can be observed from the outside (Bertaux et al., 1996).

* Corresponding author.

E-mail address: emmanuel.marcq@latmos.ipsl.fr (E. Marcq).

In this paper we present a partial analysis of the day side UV spectrum of Venus in the range 200–320 nm, as recorded by the SPICAV UV spectrometer on board ESA *Venus Express* orbiter, looking at nadir. The day side UV spectrum (in the SPICAV range 170–320 nm) of Venus is composed of two distinct parts. One is composed of natural aeronomic emissions (day-glow) due to the excitation of solar UV on an atmosphere of CO₂, and should be comparable in structure to what is observed at Mars (Leblanc et al., 2006). The other is solar radiation back-scattered by cloud particles, which is overwhelmingly more intense than the day-glow aeronomic emissions. From a practical point a view, when looking at nadir, it is impossible to detect the day-glow without setting a gain of our image intensifier that would probably damage it with the intense back-scattered radiation. This is why, for the time being, SPICAV-UV was operated with a low gain on the day side: what is recorded is the solar light back-scattered by the atmosphere of Venus, which carries information about the scattering particles, and about the gaseous phase encountered along the path of solar photons. In the wavelength range 170–320 nm covered by SPICAV-UV, the solar spectrum is influenced by Rayleigh scattering, by CO₂ pure absorption below about 200 nm, by SO₂ in two conspicuous bands (205–225 nm and 270–310 nm), by SO around 200–220 nm and by absorption in cloud particles (here it is assumed that the continuous absorption other than CO₂, SO₂ and SO is due to a contaminant of cloud particles, likely to be the famous unknown UV absorber responsible of the UV marks conspicuous at 365 nm in VMC images, for example).

The rest of this paper is organized as follows. In Section 2 are described the observations, and the data processing of SPICAV-UV spectra to retrieve the absolute brightness, then the radiance factor, or the absolute reflectance (or local albedo). In Section 3 are described the atmosphere/cloud model, the radiative transfer procedure to simulate a radiance factor for the given observation conditions, a sensitivity study and the fitting strategy to retrieve from each measured spectra (or average of spectra) a quantity of SO₂. In Section 4, the results obtained during 19 orbits are analyzed as a function of latitude, local solar time and time of observation, evidencing a sudden increase of SO₂ in early 2007. These results are compared with previous results, and are briefly discussed in terms of dynamics and photo-chemistry, with some concluding remarks.

2. Data processing

2.1. Observations

The SPICAV instrument – Spectroscopy for Investigation of Characteristics of the Atmosphere of Venus, Bertaux et al. (2007) – on-board *Venus Express* consists in three spectrometers in the UV and the IR range. In our study, we only used the UV channel whose relevant specifications in this paper are displayed in Table 1. This channel is very similar to the UV channel of the SPICAM instrument part of the payload of *Mars Express*. We refer the interested reader to Bertaux et al. (2006, 2007) for further details about the instrument.

SPICAV can be used according to several observation modes. In our study, we used exclusively *nadir mode* observations, whose

emission angles are always lower than 5°. With respect to previous space observations, our SPICAV-UV observations have four characteristics of interest:

1. The nadir viewing geometry allows to probe at larger depths in the clouds than oblique viewing.
2. The experiment is well calibrated from numerous star observations, allowing a safer interpretation of the measured absolute spectral reflectance.
3. The field of view is small (0.4 × 0.8 mrad), allowing the study on smaller scales (spatial resolution up to 72 × 144 m at a pericenter altitude of 250 km).
4. The spectrum is recorded on a multipixel detector, all wavelengths simultaneously. Signal at the center of the CCD is read and binned on 5 bands of 4 pixels lines each that are co-added so that each observation consists actually in five, mostly independent, spectra.

Up to 21 observations have been processed up to now and were available for our study. An extensive summary of the used observations can be found in Table 2. We also dismissed observations with a Solar Zenith Angle (SZA) larger than 89°. Beyond this value, the finite angular size of the Sun (~1° as seen from Venus) should be taken into account whereas our model assumes parallel incoming beams.

The quasi-polar orbit and pointing mode of the spacecraft is responsible for the fact that each observation (yielding about a thousand individual spectra) follows an almost North-to-South swath on the planet. They thus usually exhibit a very limited coverage in local time but a large one in latitude. An examination of Table 1 points out also to a major bias in our data set: due to the inclination of the *Venus Express* spacecraft orbit, the latitudinal coverage is concentrated in the northern hemisphere; in fact, we have no data at all below 30°S. On the other hand, the preliminary processing of nadir spectra requires more caution than for occultation studies, so that only the first 400 orbits could be processed up to now, which causes a lacunar coverage with respect to local time.

2.2. Pre-processing

2.2.1. Generalities

Using nadir mode above Venus' day side, SPICAV-UV measures the solar flux reflected and scattered by the very dense clouds which shroud the whole planet. Thus, the brightness spectrum $B(\lambda)$ for Venus' clouds illuminated by the Sun is defined by $B(\lambda) = R_f(\lambda) \cdot E_s(\lambda)/\pi$ where R_f is the *radiance factor* – defining the albedo A through the formula $R_f = A \cdot \cos(\text{SZA})$ – and E_s the solar flux density in photons/cm²/s/nm. E_s was taken from SOLSPEC data recomputed for Venus' orbit (Thuillier et al., 2009). On the other hand, $B(\lambda)$ can be directly obtained from SPICAV-UV measurements according to the formula from Bertaux et al. (2007): $B(\lambda) = N_{\text{ADU}}(\lambda)/S_{\text{eff}}(\lambda)G\delta\lambda\delta t p\delta\omega_l$ where N_{ADU} is the number of photons in Analog-to-Digital Units, S_{eff} the effective area (defined as $N(\lambda) = S_{\text{eff}}(\lambda)\Phi(\lambda)$ with $N(\lambda)$ the number of detected photons/s/nm and $\Phi(\lambda)$ the stellar flux in photons/s/nm/cm²) which was determined in flight by cross-calibration with IUE and HST spectra of bright UV stars (Bertaux et al., 2006), G the gain of the CCD intensifier (number of produced ADUs by one photonic event), $\delta\lambda$ the spectral width of one spectel, δt the exposure time, $\delta\omega_l$ the solid angle covered by a single line on the CCD and p the binning factor (number of CCD lines collected together). In nadir mode, all these parameters are fixed to the following values: $G = 0.056\text{ADU/event}$, $\delta\lambda = 0.548\text{ nm}$, $\delta t = 160\text{ ms}$, $\delta\omega_l = 7.98610^{-8}\text{ sr}$ (with a slit width of 50 μm) and $p = 4$. We then obtain the following expression for $R_f(\lambda)$:

Table 1
Specifications of SPICAV-UV from Bertaux et al. (2007).

Spectral range with slit	110–320 nm
Spectral sampling (center of CCD)	0.55 nm/pixel
Spectral resolution (center of CCD)	1.5 nm
Pixel FOV	40" × 40"
FOV with smaller slit	0.024° × 2.19°
Nominal temporal sampling	1 CCD reading/s
Nominal CCD configuration	5 bands of 4 lines each

Table 2
Processed SPICAV observations.

Orbit #	Obs. #	# of spectra	Latitudinal range	SAZ range	Local solar time (h)
86	7	1011	15.5–89°N	64.3–89°	7.8
100	2	995	15.9–87.7°N	43.4–89°	9.35
108	7	1481	6.5°S–77.9°N	27.9–80.3°	10.15
110	7	1481	6.4°S–77.9°N	24.7–80.2°	10.4
111	7	1481	25.6°S–15.3°N	23.0–33.1°	10.5
149	16	580	33–78.3°N	51.2–83.5°	14.6
150	16	581	33–78.3°N	52.3–83.8°	14.7
151	3	1782	14.2°S–78.4°N	42.2–84°	14.8
152	3	1780	14.1°S–78.3°N	43.8–84.2°	14.9
153	3	1780	14.1°S–78.3°N	45.4–84.5°	15
174	10	1660	11.4°S–72.9°N	79.4–88.9°	17.3
249	1	1630	6.8–88.4°N	19.7–89°	13.3
261	7	1717	0.2–73.4°N	38.2–74.4°	14.5
310	19	991	17.2–89.1°N	65–89°	7.7
325	20	976	17.5–88.0°N	43.1–89.0°	9.35
326	20	975	17.6–87.9°N	41.7–89.0°	9.5
328	17	971	17.7–87.7°N	39.0–88.9°	9.7
332	19	1270	5.0–87.6°N	29.1–88.9°	10.1
334	18	1267	5.1–87.4°N	26.0–88.9°	10.3

$$R_f(\lambda) = \pi N_{\text{ADU}}(\lambda) / E_S(\lambda) S_{\text{eff}}(\lambda) G \delta \lambda \delta t p \delta \omega_i$$

R_f is designed so that it is intrinsic to the observed object – Venus' upper atmosphere. In particular, it is totally independent from the spectral signature of the Sun. Therefore, our pre-processing consists in computing R_f from raw SPICAV-UV spectra according to the following stages:

1. Subtraction of dark current (DC).
2. Removal of electronic noise (EN).
3. Flat-field correction (FF).
4. Subtraction of stray light (SL).
5. Pixel-to-wavelength assignment (PW).

The raw data consist in integer values of ADU on each spectral pixel (see blue curve on Fig. 1). Values at pixel numbers over 250 ($\lambda < 180$ nm) are very low because of the weak solar flux in this spectral range and absorption by CO₂. Only pixel numbers ranging from 9 to 391 are usable.

2.2.2. Dark current

The required information about dark current can be retrieved from the masked pixels. When continuously observing a fully dark background, pure dark currents could be measured for all pixels and are noted DC_i for the i -th pixel. On the other hand, the

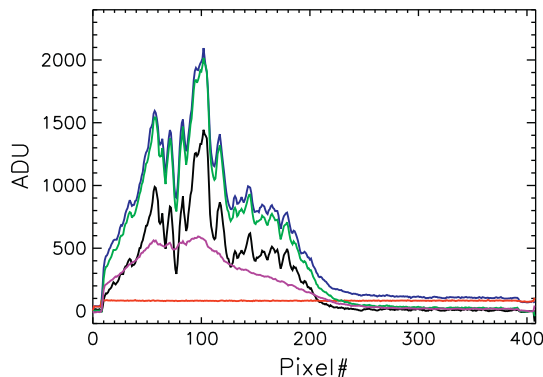


Fig. 1. Treatment of a raw signal (blue) taking into account dark current (DC, red), relative flat-field correction (green), electronic noise and stray light (SL, magenta). Final stage is shown in black. (For interpretation of the references to color in this figure legend, the reader is referred to the web version of this article.)

averaged dark current in the mask pixels is noted M . The monitoring of DC_i and M with time enabled us to establish a linear variation of DC_i with respect to M : $DC_i(t) = A_i M(t) + B_i$. Once the coefficients A_i and B_i were computed for each pixel, dark current could be retrieved and subtracted for all observations provided we know the dark current under the mask M – see red curve of Fig. 1.

2.2.3. Electronic noise

A close examination of the raw signal showed us that spectra were perturbed by a sinusoid-shaped electronic noise (amplitude: ~ 3 ADU, period: ~ 14 pixels). The relative phase of this perturbation differs from spectrum to spectrum. We then proceeded to fit this component in a spectral region where the signal is the lowest (pixel numbers ranging from 250 to 391) by comparing the actual signal with a signal smoothed over 15 pixels (so that we could take actual long-scale variations of the signal into account). The fitted wave was finally removed from all parts of the signal.

2.2.4. Flat field

In order to study the flat field of the CCD matrix we used day-side nadir observation from the pericenter of orbit #284 so that we minimized the influence of horizontal variations in the field of view. Spectral resolution was intentionally downgraded by removing the slit so that the spectral signature of trace gases would not be seen. The image recorded by the CCD then yields the PRNU (photo-response nonuniformity). For local study of the PRNU, we smoothed the image on a distance of 11 pixels. Ratios of the raw image to the smoothed one yields the relative flat field (RFF) distribution on the 408×288 matrix. Depending on the binning factor p and actual CCD lines used for the scientific measurements, each signal is divided by the corresponding RFF (see green curve in Fig. 1).

2.2.5. Stray light

The spectrometer slit exhibits two different widths: narrow ($50 \mu\text{m}$) for row numbers below 190 and wide ($500 \mu\text{m}$) above. Nadir observations use exclusively the narrow part of the slit. However, there is significant stray light coming from the wider part of the slit by scattering through the MgF₂ window of the image intensifier. Estimation of this stray light was performed using a specific limb observation with the slit perpendicular to the horizon and limb light illuminating only the wide part and is shown in Fig. 1 in magenta. We could then record samples of pure stray light on the CCD lines in the narrow part, looking at the sky well above

the limb. The brightness level of the stray light had to be tuned to match the observed signal so that the net signal for pixels numbered over 220 was as small as possible. The result is shown in the black curve of Fig. 1.

2.2.6. Pixel-to-wavelength assignment

The function $i \rightarrow \lambda_i$ had to be defined for each spectrum independently because of its drift with observation time. After the four aforementioned processing stages, the spectra (as N_{ADU}) are compared to the expected solar spectrum (and especially the solar lines whose position is well known from other sources) $F_s(\lambda) = E_s(\lambda) \cdot S_{\text{eff}}(\lambda)$ convolved by the point-spread function (PSF) of the instrument. This PSF is itself varying with λ , and is Voigt-shaped (Villard, 2008). It is then broader than the typical Gaussian due to scattering in the MgF_2 blade. The parameters of the Voigt PSF – Gaussian-like core and Lorentzian-like far wings – were fitted using the spectra of a dot-like calibration star; its Full Width Half Maximum (FWHM) ranges from 3 pixels in the middle of the CCD to 5 pixels on the edges. Fine tuning of $i \rightarrow \lambda_i$ is achieved through length minimization of the candidate $R_f(\lambda_i) = N_{\text{ADU}}(i)/F_s(\lambda_i)$. Assuming a quadratic variation of λ_i with respect to pixel number i , the bumps originating in the approximate cancellation of solar lines in the ratio could be decreased using an iterative Richardson–Lucy algorithm (Lucy, 1974) for fitting the three quadratic parameters. The result can be seen in Fig. 2.

2.2.7. Computation of random error bars

Assuming a Poisson statistics of photons detections, we estimated that the variance V followed the empirical relation $V(N_{\text{ADU}}) = 0.0713 \cdot N_{\text{ADU}}$ at $G = 0.056$. The variance for R_f was then computed according to the general relation:

$$V(R_f) = \sum_j V(x_j) (\partial R_f / \partial x_j)^2$$

where x_j is a generic label for the variables of R_f : N_{ADU} , E_s , S_{eff} , G , etc. The resulting error bars $\varepsilon(\lambda) = \sqrt{V(R_f(\lambda))}$ are shown e.g. in Fig. 10. The minimal extent of the error bars is about 1–2%, and their magnitude is much higher at wavelengths less than 220 nm due to the very low signal-to-noise ratio (SNR) in that spectral range.

2.2.8. Comparison with analogous observations

A sample of processed absolute albedo is shown in Fig. 3, along with that measured by early observations performed with OAO-2 – Orbiting Astronomical Observatory 2 spacecraft, Wallace et al. (1972). To our knowledge, there are no published absolute albe-

does derived from PVO/UVS. The OAO-2 spectrum was scaled to SPICAV at 240 nm for comparison. Discrepancies are large past 250 nm with OAO-2 not observing the strong decrease with wavelength seen by SPICAV, but the calibration of SPICAV-UV was based on various bright UV stars observed in-flight, and therefore more trustworthy than OAO-2. Also, one should note that the absolute UV spectrum of the Sun is now better known than during the early 1970s – our choice of reference spectrum (Thuillier et al., 2009) illustrates this point.

3. Description of the model

The goal of our model is to provide synthetic radiance factors across the 170–320 nm range. Considering the high values of SZA in some of our observations (see Table 2), a radiative core able to cope with spherical geometry was required. As a consequence, we have chosen SPS-DISORT as a radiative transfer core code, a pseudo-spherical adaptation of the better-known DISORT code (Stamnes et al., 1988) which takes into account the spherical geometry only for the incident and emergent beams. By setting the incident beam power to unity, the synthetic radiance factor at a given wavelength is given by π times the outgoing zenithal brightness at the topmost layer. Seven-hundred-and-fifty such radiance factors are computed with a 0.2 nm wavelength step so that sampling is not an issue with the spectral resolution of about 1.5 nm. At low values of SZA, SPS-DISORT were compared to simpler plane-parallel radiative cores such as SHDOM or a simple, home-designed Monte-Carlo code. Results were very similar up to a relative accuracy of 10^{-2} , better than our observational S/N ratio.

The venusian atmosphere is modeled from an altitude of 50 km up to 110 km, and divided in 31 homogeneous, 2 km-thick layers. The temperature profile was extracted from VIRA-2 (Moroz and Zasova, 1997), and hydrostatic equilibrium was assumed to compute density and pressure profiles. Even if the temperature profile is variable at these altitudes, temperature is not a critical input of our model and departures up to 10% (20 K) of this reference profile will not affect the synthetic spectra significantly. Opacity sources taken into account are of two kinds: aerosol particles and gaseous species.

After computation, the radiance factors have been convolved for a straightforward comparison with the observations. The solar spectrum we use has been taken from Thuillier et al. (2009) and multiplied by the SPICAV spectral sensitivity function.

3.1. Aerosols

Aerosol particles were assumed to be spherical so that computations according to Mie theory could be applied. The refractive

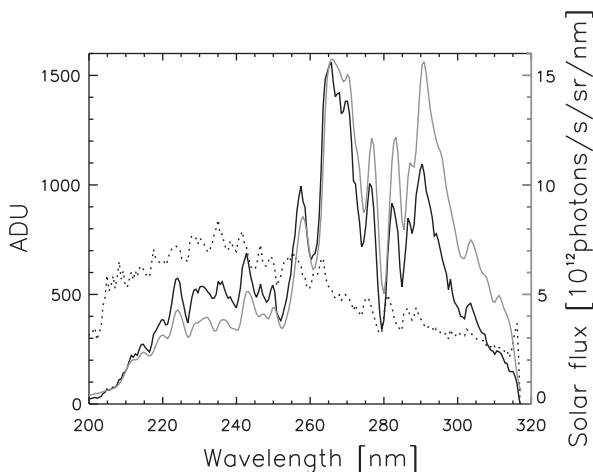


Fig. 2. Spectra of a measured signal N_{ADU} (black), radiance factor R_f (dotted) and solar flux F_s (gray). Several bumps on R_f are “ghost solar lines” due to the misalignment of λ_i (particularly near $\lambda = 245, 260$ or 280 nm).

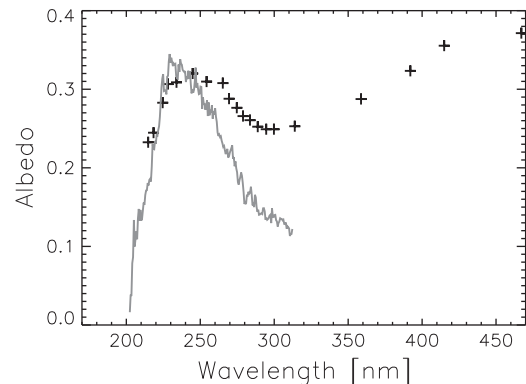


Fig. 3. A UV absolute spectral reflectance measured by SPICAV-UV during orbit #174 in 2006 at low latitude, compared to early observations with OAO-2. The OAO-2 (Wallace et al., 1972) are normalised at 240 nm to SPICAV measurements.

index was taken from E.P. Shettle from the Naval Research Laboratory and is representative of the main constituents 75% H₂SO₄ and 25% H₂O at 215 K: $n(\lambda) = (1.587 - 3.05 \times 10^{-4} \lambda [\text{nm}]) + i(1.07 \times 10^{-8})$. An extra imaginary index was also given as an input to the model to account for the unknown UV absorber, assumed to be part of the condensed phase.

It was found that the decreasing spectral slope with increasing wavelength of our observed radiance factors could not be entirely due to Rayleigh scattering. We therefore assumed that spectral variations of the single scattering albedo of the aerosols was the other contributing process causing this spectral slope. Matching both the average albedo and spectral slope, we could fit a simple exponential variation of the imaginary index of the particles: $n_i(\lambda) = 1.8 \times 10^{-6} \exp(-\lambda/33.84 \text{ nm})$. This value is much greater than the 1.07×10^{-8} value for H₂SO₄ given by Shettle. This increasing absorption could be related to the unknown UV absorber whose absorption reaches its maximum near 360 nm. The spectral range of SPICAV prevents us from confirming this, but other instruments on-board *Venus Express* could do this in a near future (VIRTIS Visible, VMC).

A bimodal distribution of the aerosols was implemented: mode 1 particles ($\bar{r} = 0.24 \mu\text{m}$, $\sigma = 0.25$) is found in the upper cloud region and in the upper haze, whereas mode 2 particles ($\bar{r} = 1.1 \mu\text{m}$, $\sigma = 0.23$) account for most of the opacity in the upper cloud deck. Mode 3 particles are normally only found at the bottom of modeled altitude range (middle cloud deck), in a region reached by little incident light so that we could represent their effect by increasing the density of mode 2 particles in the 50–56 km region. $\sigma_{\text{ext}}(\lambda)$, $\varpi_0(\lambda)$, $g(\lambda)$ and phase functions $\varphi(\theta, \lambda)$ were therefore computed for each wavelengths and both modes 1 and 2 following Mie theory. The high values of the computed asymmetry parameter g required the use of the Delta-M approximation (Wiscombe, 1977) in the radiative transfer model, using 144 coefficients for the Legendre expansion of the phase functions. Computed values of ϖ_0 and g for both modes are shown in Fig. 5.

The upper clouds consist in a mix of mode 2 and mode 1 particles, the extinction coefficient of each mode being vertically uniform between 56 km and the upper cloud/upper haze boundary. In the upper haze region above, only mode 1 particles are found with an exponentially decreasing extinction according to a scale height H_1 . Our standard haze and clouds parameters as well as modal distribution are detailed in Table 3.

3.2. Gaseous components

Gaseous species considered in our study were major species like CO₂ and N₂ on the one hand, and on the other hand SO₂ and SO were the only minor species considered. Major species mixing ratios were assumed to be uniform with volumetric fractions $f_{\text{CO}_2} = 0.965$ and $f_{\text{N}_2} = 0.035$ respectively. Rayleigh scattering was

duly computed for them, according to the following cross-section formulae from Snee and Ubachs (2005) where λ is in nanometers: $\sigma_{\text{ray}}(\text{CO}_2) = 12.4 \times 10^{-27} (532.24/\lambda)^4 \text{ cm}^2$ and $\sigma_{\text{ray}}(\text{N}_2) = 5.1 \times 10^{-27} (532.24/\lambda)^4 \text{ cm}^2$.

Absorption by CO₂, SO₂ and SO was also dealt with. We took into account the temperature dependence for the cross-sections, albeit only for CO₂ whose cross-sections were extracted from (Parkinson, 2003). SO₂ cross-sections were taken from Wu et al. (2000) in the 170–297 nm range and from Rufus et al. (2003) for the remaining 297–320 nm interval. Recent SO measurements are hard to find in the databases; we scanned the printed plots from Phillips (1981) in the 190–230 nm range, and extrapolated the cross-section out of this interval with a best-fitting parabola (λ in nanometers):

$\log_{10}(\sigma_{\text{abs}}(\text{SO}) [\text{cm}^2]) = -2.276 \times 10^{-3} \lambda^2 + 0.911 \lambda - 107.94$. All these cross-sections are shown in Fig. 4.

Vertical profiles of SO₂ and SO are exponentially decreasing with increasing altitude both below and above the upper cloud boundary. According the average value from Sandor et al. (2010) and UV occultations from D. Belyaev, we tied SO mixing ratio to 10% of SO₂. Also, SO₂ mixing ratios q_{SO_2} is capped at a maximal value of 150 ppmv which is the known mixing ratio in the source region (the lower atmosphere). Both species share the same scale height (see Table 3). This common scale height was taken from observations of SO₂ vertical profiles in solar occultations with SPICAV/SOIR spectrometer on-board *Venus Express* (Belyaev et al., 2008). We assumed that SO followed the same scale height as SO₂ for lack of relevant data.

3.3. Sensitivity study

3.3.1. Sensitivity towards SO₂ and SO column densities

Fig. 6 (solid line) shows the ratio of synthetic radiance factors with and without any minor species (SO and SO₂). One can immediately notice the presence of the two absorbing bands of SO₂ since SO shares the 215 nm band, it cannot be distinguished easily from SO₂ at a relatively low, SPICAV-like spectral resolving power – in consequence, we shall not further discuss SO retrieval in the subsequent sections.

A possible concern is the fact that Venus' upper cloud and haze is strongly variable with time and latitude. Any alteration in cloud properties such as the ones in Table 3 could alter the spectral sensitivity to SO₂ content. To quantify this perturbation, we have proceeded to a similar ratio with the same column density of SO₂ and SO above the unitary optical depth level (z_1 such as $\tau_{\text{aerosol}}(z_1) = 1$) but using cloud parameters more likely encountered at higher latitudes (mainly, a lower upper cloud top and thicker haze) referred

Table 3
Standard parameters used in the synthetic low latitude and polar cases.

	Low-latitude	Polar
<i>Mode 1</i>		
$\tau_1(z > \text{UCB})$	0.7	2
$H_1(z > \text{UCB})$ (km)	4.28	1
<i>Mode 2</i>		
Upper cloud/upper haze boundary (UCB) (km)	72	65
$\tau_2(50 < z < 56 \text{ km})$	9.72	9.72
$\tau_2(56 \text{ km} < z < \text{UCB})$	5.12	5.12
<i>Other</i>		
$z(\tau_{\text{aerosol}} = 1)$ (km)	71	66
$H_{\text{SO}_2} (= H_{\text{SO}})$ (km)	3	1
Solar Zenith Angle (SZA) (°)	45	75

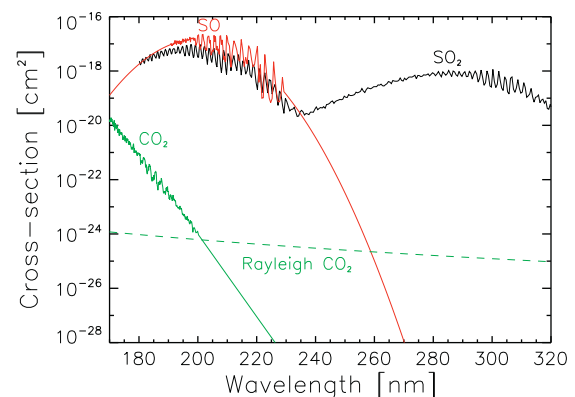


Fig. 4. Cross-sections of CO₂, SO₂ and SO. Rayleigh scattering cross-section of CO₂ is also shown (dashed line).

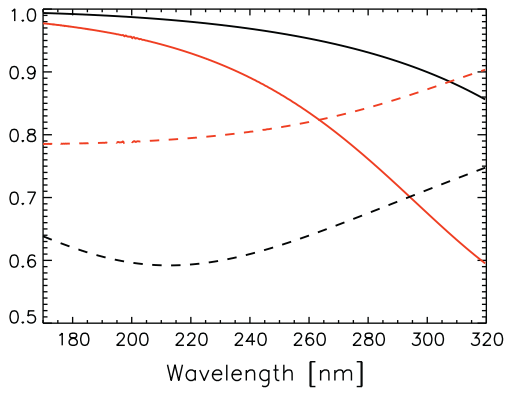


Fig. 5. ω_0 (solid lines) and g (dashed lines) for mode 1 (black) and mode 2 (red) particles using the fitted refractive index from Section 3.1. (For interpretation of the references to color in this figure legend, the reader is referred to the web version of this article.)

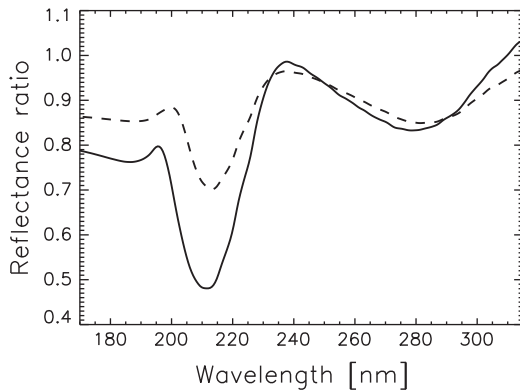


Fig. 6. Ratios of synthetic radiance factors ($N_{\text{SO}_2} = 30 \mu\text{m-atm}/N_{\text{SO}_2} = 0 \mu\text{m-atm}$) in the standard case (solid) and in the polar case (dashed).

as a *polar case* in Table 3. We then scaled each other at a common average value since our fitting algorithm is only sensitive to the shape of the spectral ratio.

The result is shown in the dashed line in Fig. 6. The 215 nm band is less pronounced, which is expected since it lies in the wing of a CO_2 band and thus exhibits a direct dependency to CO_2 pressure (and therefore absolute altitude levels); the increased depth in the polar case makes SO_2 less noticeable in this band. On the other hand, the 280 nm band is strikingly similar for both cases, provided that column density of SO_2 above z_1 is kept the same notwithstanding any realistic variation of clouds and hazes. Thus, a proper fit in this band yields a robust estimate of the overall SO_2 content, and in the subsequent sections, we shall only use the better known equatorial aerosol parameters for the fit of SO_2 bands.

3.3.2. Sensitivity towards upper haze optical depth

Fig. 7 shows the ratios of synthetic radiance factors with the same column densities of SO_2 above z_1 but with varying optical depth τ_1 of mode 1 particles (representative of an optically thicker or thinner upper haze). Note that this implies a larger SO_2 mixing ratio at any given altitude with increasing τ_1 since z_1 (above which the column density of SO_2 is considered) will be higher then. The 215 nm band still exhibits some variability for the same reason already discussed in Section 3.3.1: its direct sensitivity to the actual altitudes (not relative to the aerosol opacities). But at constant column density, the 280 nm band is almost not noticeable in the ratio, since the probed content is similar in both situations. On the other hand, the ratios exhibit a different slope with varying τ_1 which is

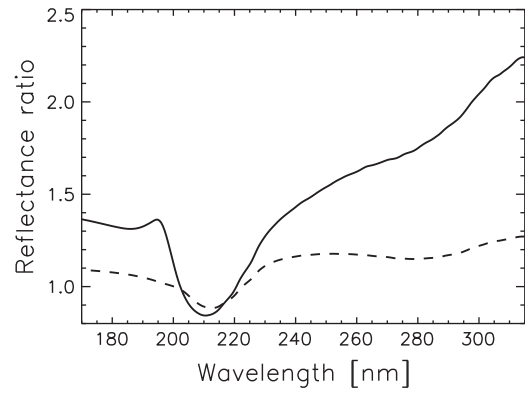


Fig. 7. Ratios of synthetic radiance factors ($\tau_1 = 2/\tau_1 = 0.7$) in the standard case (solid) and in the polar case (dashed).

expected because the contributions of mode 1 and mode 2 particles – whose $\omega_0(\lambda)$ and $g(\lambda)$ differ – vary with τ_1 since τ_2 is kept constant. Note that in the polar scenario, the slope is less pronounced, mainly because the high values of SZA results in mode 1 particles always contributing most to the aerosol opacity.

3.3.3. Sensitivity towards minor species scale height

Fig. 8 shows the ratios of synthetic radiance factors with the same column density and aerosol parameters (low latitude in solid line, polar case in dashed line), but with a varying scale height for minor species. The situation is quite similar to the one observed in Section 3.3.2: the narrow band depth is different with the scale height, whereas the broader band near 280 nm is almost not affected since it probes the SO_2 column density down to z_1 as previously mentioned.

3.3.4. Column densities versus mixing ratios

Sections 3.3.1–3.3.3 emphasize the column density of SO_2 above $z_{\tau=1}$ as our primary observable parameter. In order to compare our results to previous measurements, we may translate the column densities into vertical profiles $q_{\text{SO}_2}(z)$ and $q_{\text{SO}_2}(z)$ (in ppmv). This translation depends on our assumption of the vertical profiles' shape, but even more on the haze and cloud extinction profiles described in Table 3: very small amounts of SO_2 can be detected provided it is located “above” most of upper haze's opacity and, conversely, relatively high amounts of SO_2 would be unnoticed if “buried” below the clouds; in fact we know that substantial amounts of SO_2 actually lie within the clouds of Venus from *in situ* measurements (see Fig. 24 from Bertaux et al., 1996). We therefore insist that our primary observable parameters regarding gaseous species are the column densities above a certain level

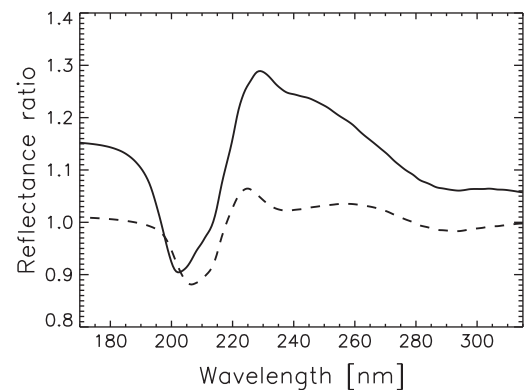


Fig. 8. Ratios of synthetic radiance factors ($H_{\text{SO}_2} = 5 \text{ km}/H_{\text{SO}_2} = 1 \text{ km}$) in the standard case (solid) and in the polar case (dashed).

(defined by the cloud properties), and that the mixing ratios that we shall give later are derived parameters relying on the assumptions described in this paragraph, and should be considered as order-of-magnitude estimates. Assuming the SO₂ vertical profiles described in Section 3.2, the conversion factors between SO₂ column density above z_1 and mixing ratio at 70 km (40 mbar) range from 13 ppb per $\mu\text{m-atm}$ ($\tau_1 = 0.5$) to 150 ppb per $\mu\text{m-atm}$ ($\tau_1 = 2$). Considering the average value of τ_1 at lower latitudes ($\tau_1 = 0.7$), a rough estimate of the conversion factor from column density to mixing ratio at 70 km is 20 ppb per $\mu\text{m-atm}$ ($1\mu\text{m-atm} = 2.69 \times 10^{15}$ molecules/cm²).

3.4. Fitting strategy

3.4.1. Choice of fitted parameters

The presence of two separate bands in the spectral ratios enable us to fit up to two parameters. We thus have to pick up two parameters in the following list:

- SO₂ column density (N_{SO_2}).
- SO column density (N_{SO}).
- Upper haze opacity (τ_1).
- SO₂ (and SO) scale height (H_{SO_2}).

SO₂ column density is an obvious choice, and we already discarded the possibility of recovering SO mixing ratio from our spectral data with a reasonable accuracy. We then are left with two choices for the second fitted parameter: τ_1 or H_{SO_2} . Both alter the depth of the 215 nm absorption band relatively to the broader one as well as the spectral slope past 230 nm albeit in different ways (see Figs. 7 and 8). The resulting degeneracy prevents us to retrieve any of them with a reasonable accuracy unless further input is provided by other instruments. Moreover, there must be some variability of the SO/SO₂ ratio that could also alter the relative depth of the two absorption bands, thus adding even more degeneracies to our problem. Our choice finally settled on τ_1 as the secondary fitted parameter for two reasons. First of all, H_{SO_2} could already be better constrained through SOIR occultations (Belyaev et al., 2008) and thus be considered as an external input for our model. Also, the agreement between synthetic and observed radiance factors was better in the (N_{SO_2}, τ_1) subspace than in the ($N_{\text{SO}_2}, H_{\text{SO}_2}$) one, yielding more precise estimates of N_{SO_2} through a smaller χ^2 .

3.4.2. Algorithm

Assuming the usual metric $d(S, E)$ on the spectra's function space:

$$d(S, E) = \sum_{i=1}^N \left[\frac{E(\lambda_i) - S(\lambda_i)}{\varepsilon(\lambda_i)} \right]^2$$

where E , S and ε stand respectively for observed radiance factor, synthetic radiance factor and random error on the observed radiance factor, we have minimized d with respect to S in order to retrieve SO₂ column abundance. We used the Levenberg–Marquardt algorithm developed by Markwardt (2009) in order to find our best estimates and their error bars. In order to account for local variations of the albedo (the well-known UV contrasts), we let the algorithm free to scale the synthetic spectrum S in order to minimize $d(E, S)$ – in other words, we tried to fit the shape of the reflectance rather than its absolute value. In order to ensure that the algorithm found the meaningful minimal value of d instead of any local minimal value, we proceeded as follows: first, we initiated the iterative algorithm with starting values not far from the average: $N_{\text{SO}_2} = 10 \mu\text{m-atm}$, scaling factor set to 1. Then, we minimized d with respect to N_{SO_2} and τ_1 using both bands between 210 and 300 nm.

In order to increase the speed of the fitting process, synthetic radiance factors are precomputed in a tridimensional grid: N_{SO_2}

and τ_1 which are fitted, and SZA whose variations should be taken into account properly. The estimator then proceeds to a trilinear interpolation to yield synthetic radiance factors matching the prescribed inputs of the model.

One could also point out that some difficulties such as the unknown spectrum of the UV absorber or some instrumental issues could be at least partially cancelled if we decided to fit not the absolute radiance factors but *ratios* of radiance factors using for example a low-content, equatorial observation as a reference. Actually, we followed this approach in our preliminary work, and the results we obtained are fully consistent with the ones shown hereafter. Examining ratios is also a good way to investigate for possible discrepancies between our model and the observations – such comparisons are shown in Figs. 9, 11 and 12. Nevertheless, we obtained our final results by fitting absolute radiance factors because of the supplementary information that could be extracted from it: an estimation of the optical properties of the aerosols, and especially their imaginary refractive index (see Section 3.1) as well as having access to the absolute abundance of SO₂ instead of being constrained to discuss its relative variations. Also, from a mathematical point of view, there is no difference between fitting radiance ratio instead of absolute radiance factors. Although the spectral weighting function in the estimation of $d(S, E)$ is different in both cases, the random error $\varepsilon(\lambda)$ is changed in such a way that it yields the same value for $d(S, E)$.

3.4.3. Estimation of uncertainty

Random noise, estimated by the $1 \cdot \sigma$ uncertainty given by the Levenberg–Marquardt algorithm, is usually one order-of-magnitude below the statistical standard deviation of the results obtained after fitting separately the five bands of the CCD recorded simultaneously. Assuming that these five bands provide measurements of the same region on Venus and should therefore yield the same value for N_{SO_2} , we can consider that this standard deviation is a better estimator of the total error (random and systematic) of our fits. Incidentally, the minimal statistical dispersion is obtained with a binning factor of about 20 – that is, co-adding 20 spectra at a time to improve the S/N ratio at the expense of spatial/temporal resolution. This yields about 50 independent fits of N_{SO_2} per orbit that we will discuss in the next section.

4. Results

4.1. Comparison between data and their fits

4.1.1. Identification of SO₂ variations on spectral ratios

Fig. 9 shows the ratios of two SPICAV-UV spectra (an equatorial and a polar one) along with a ratio of two synthetic spectra (with

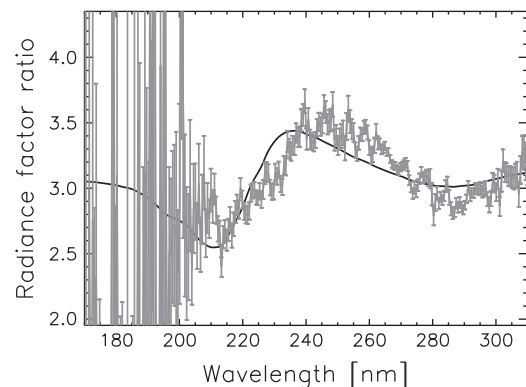


Fig. 9. Gray: ratio of two SPICAV-UV spectra, equatorial/polar on orbit #174; black: ratio of two synthetic spectra computed from our radiative transfer model, with SO₂/without SO₂.

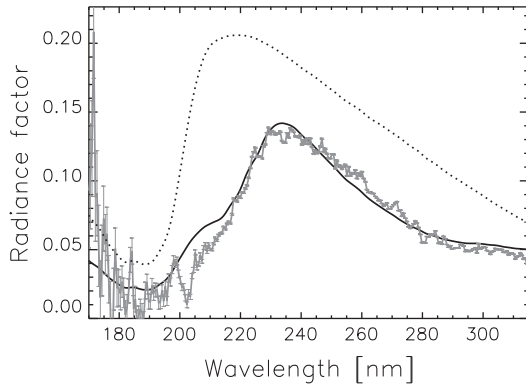


Fig. 10. Observed radiance factor around 20°N during orbit #310 and its best fit with SO₂ (solid line). The fit without any SO₂ is shown in a dotted line.

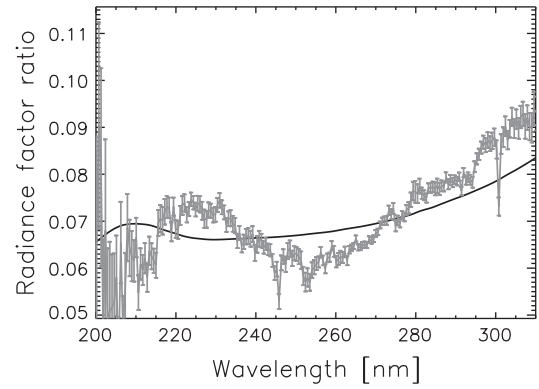


Fig. 12. Observed relative radiance factor (using the same reference as in Fig. 11) around 80°N during orbit #328 and its best fit with SO₂ (solid line).

and without SO₂). An interest of comparing ratios instead of absolute radiance factor is that some sources of uncertainty cancel out in this way – most notably solar UV variations with respect to our reference spectrum and poorly constrained upper cloud and hazes. Such an approach was convincingly done by Stewart et al. (1979, their Fig. 1) with PVO/UVS spectra. This Fig. 9 summarizes an unambiguous finding of ours, namely the confirmation of SO₂ variations with respect to latitude, with more SO₂ detected at lower latitudes compared to higher latitudes. We shall give quantitative estimates in the following section using the algorithm described in Section 3.4.2.

4.1.2. Main situations encountered

An example of fit that we obtain at low latitudes is shown in Fig. 10: the presence of both SO₂ band is clearly visible, and the fit is very good at wavelengths greater than 220 nm. The small disagreement at shorter wavelength can be due to a large number of causes: variation in the SO/SO₂ ratio, scale height, cloud top. We can also note a yet unidentified absorption feature at about 205 nm, whose identification is beyond the scope of this paper.

The situation at higher latitudes is more complex, and better understood when looking at spectral ratios. Some ratios are well fitted with a modest content in SO₂ as shown in Fig. 11. But others are not satisfactorily fitted (see Fig. 12) and although some SO₂ should be present to account for the relative low ratio near 210 nm, we are convinced that another absorber is present, peaking near 250 nm. At the time of writing this paper, we suspect that this absorber might be gaseous O₃ above the clouds, but the required column density of O₃ required is much higher than most

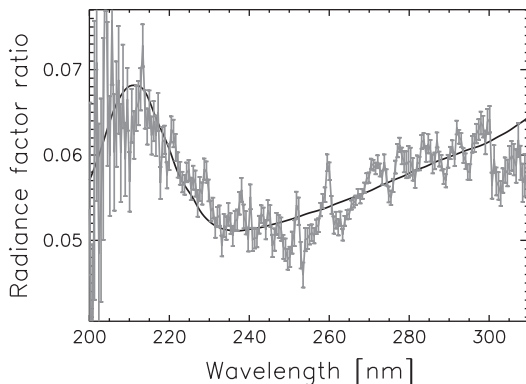


Fig. 11. Observed relative radiance factor (using a low SO₂ equatorial spectrum from orbit #111 as a reference) around 70°N during orbit #174 and its best fit with SO₂ (solid line).

models predict (Franck Mills, private communication) so that this identification is only tentative at this stage. The correlation between SO₂ and this 250-nm feature is uni-directional: most polar spectra with a high SO₂ content exhibit the 250-nm absorption feature, but not the other way around.

Further investigation on this issue is beyond the scope of this paper but will be done in the near future.

4.2. SO₂ column densities

4.2.1. Latitudinal variations

The latitudinal variations of the retrieved sulfur dioxide column densities are shown in Fig. 13. First of all, significant variations of the SO₂ content can be seen from one orbit to another, pointing out longitudinal and/or temporal variability of SO₂. Furthermore, even when considering any single orbit, medium-scale variations of N_{SO₂} are unambiguously detected within 5° of latitude, which corresponds to a typical horizontal length of several hundreds of kilometers. Also, for most of the orbits, typical values for N_{SO₂} lie between 5 and 50 μm-atm (median around 10 μm-atm) at lower latitudes.

About a third of the orbits (the most recent ones) exhibit a noticeable gaseous content even at high latitudes, comparable with the low latitude values. However, these orbits exhibit spectra that are yet poorly fitted as already mentioned in Section 4.1.2, so that the actual content in SO₂ may be actually lower – but still more abundant than in other polar regions.

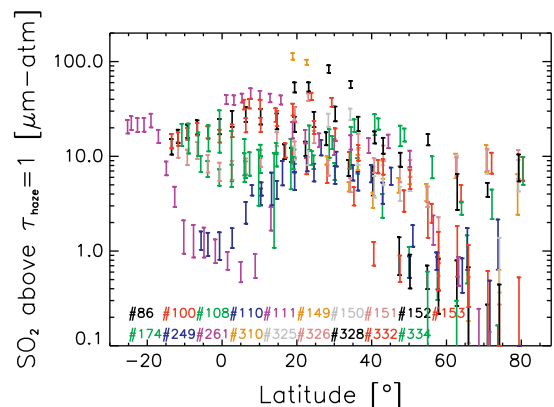


Fig. 13. Variations of N_{SO₂} with latitude for several orbits. Each orbit is represented by error bars of different color indicated by orbit number. There are 19 orbits, spread over a period of 334 – 86 = 248 days. Note the logarithmic scale, required to display the huge variability of SO₂ (two orders of magnitude).

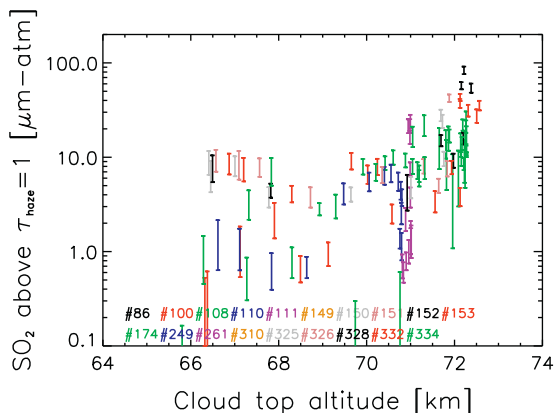


Fig. 14. Variations of N_{SO_2} with cloud top altitude for several orbits.

4.2.2. Correlation with cloud top altitude

It is already known that the upper cloud top altitude exhibits a pronounced latitudinal behavior (Ignatiev et al., 2009; Titov et al., 2008), ranging from about 65 km near the poles up to about 74 km near the equator and mid-latitudes. Using data obtained from CO_2 bands between 1.4 and 1.65 μm with SPICAV-IR for the same orbits, we were able to examine the correlations between the cloud top altitude and N_{SO_2} . Results are shown in Fig. 14. A positive correlation between cloud top altitude and N_{SO_2} can be clearly seen, as well as the separation between polar sulfur-rich and polar sulfur-poor regions already discussed. Such a correlation is expected considering the trend with latitude seen on Fig. 13 and the known behavior of cloud top altitude with latitude. Nevertheless, this correlation of N_{SO_2} with cloud top altitude seems of better quality (with “narrower branches”) and more convincing than the correlation of N_{SO_2} with latitude. This suggests that some dynamical phenomenon is able to induce a simultaneous lowering of cloud top altitude and decrease of N_{SO_2} at high latitudes.

This correlation might be believed spurious due to the distortion of UV spectra caused by the dramatic changes in the upper clouds and decks in the polar region compared with the more familiar equatorial region. However this would be unlikely considering the arguments given in Section 3.3.1. Furthermore, this latitudinal trend has also been seen using solar occultations at high spectral resolution in the infrared by Belyaev et al. (2008), and their study does not have to cope with the same degeneracy issues as ours. This correlation is then unlikely to be spurious.

4.2.3. Other correlations

Figs. 15 and 16 show respectively the SO_2 column densities in function of local solar time and observation date. A steady decrease of the maximal SO_2 content with local solar time can be seen in Fig. 15 and could be due to photochemical destruction of SO_2 during its advection by the super-rotation from the morning to the evening terminator. However, the computed effective lifetime of SO_2 in this case is one order-of-magnitude inferior to the one derived from photochemical models (Mills and Allen, 2007) – assuming a 100 m/s zonal wind speed, we find 10^5 s instead of 10^6 s – which casts further doubt on this interpretation.

Fig. 16 provides a more convincing interpretation. Due to the orbital parameters of *Venus Express*, various longitudes (and therefore “time zones”) are not observed randomly, but with a small longitudinal drift orbit after orbit. The variation with local solar time can thus be understood as a spurious consequence of an actual variation of SO_2 between 2006 and 2007: minimal and maximal mixing ratios of SO_2 appear quite constant until orbit #249. From orbit #310 onwards, mixing ratios of SO_2 are always higher, at least for minimal values in any orbit and also for the median and

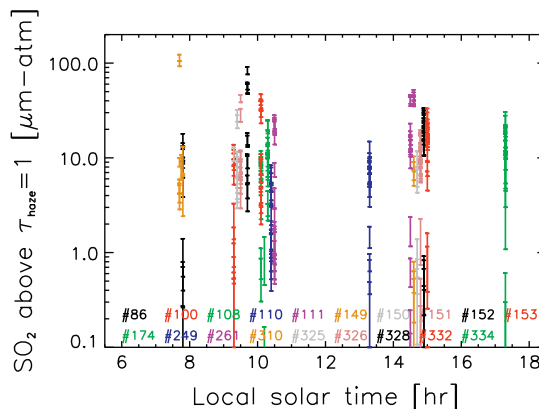


Fig. 15. Variations of N_{SO_2} with local solar time for several orbits.

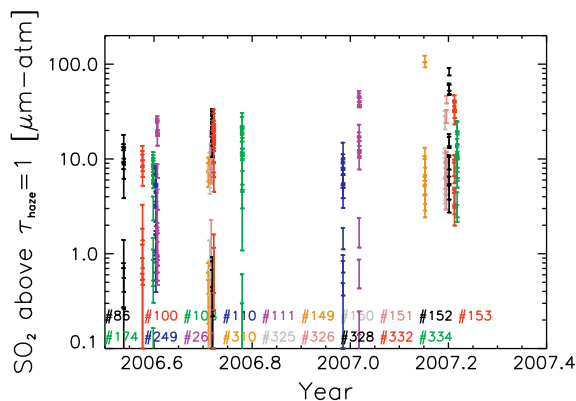


Fig. 16. Variations of N_{SO_2} with terrestrial year for several orbits. Note the sudden increase in SO_2 in early 2007.

maximal values although they are harder to assess statistically. This 2007 increase may be more noticeable in Fig. 17, where two different colors are used for orbits before and after January 2007. Some global (or, at least, northern) SO_2 enrichment event at cloud top level must therefore have occurred in the first months of 2007.

4.3. Discussion

4.3.1. Comparison with previous measurements

To compare with previous studies, we have to translate our column densities into mixing ratios at cloud top according to the relation given in Section 3.3.4. We then have mixing ratios for SO_2 at $P = 40$ mbar ranging usually from 0.1 to 1 ppmv (and sometimes rising above 1 ppmv during mornings), whereas in the polar region mixing ratios are usually below 50 ppbv except for recent orbits after the early 2007 event for which we find 0.1–0.2 ppmv.

These mixing ratios/column densities lie within the usual range of for SO_2 since its UV signature was evidenced in 1979 (Barker, 1979; Esposito et al., 1979; Conway et al., 1979; Stewart et al., 1979; Parisot et al., 1986; McClintock et al., 1994). Our relatively high average value (about 0.5 ppmv) indicates that the long-term decrease in SO_2 since its detection in 1978 (Na et al., 1990) stopped between 1990 and 2006; some SO_2 replenishment of the upper troposphere/lower mesosphere may then have occurred during this time interval since our SO_2 retrievals are also higher than those of Na et al. (1990).

In this long-term context, the sudden enrichment between orbits #260 and #310 may be one among many sporadic events

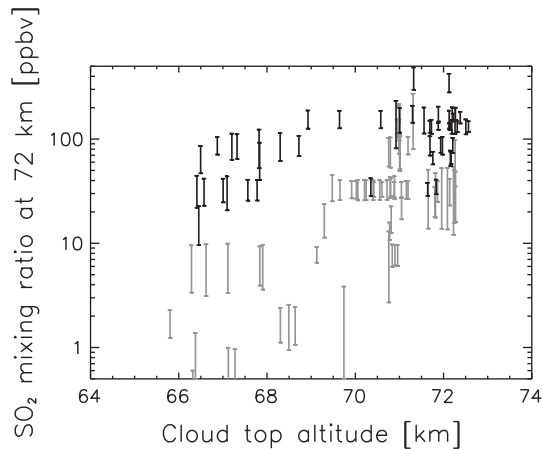


Fig. 17. Variations of SO₂ mixing ratio at 72 km with cloud top altitude for several orbits. Gray is used for orbits of 2006 and black for 2007.

responsible for halting the decennial decrease observed prior to 1990 and for changing the latitudinal pattern observed before, since the present situation (low latitude regions richer in SO₂ compared to high latitudes) is also in disagreement with the one found by Na et al. (1994) and Zasova et al. (1993). Nevertheless, more recent measurements of SO₂ by Belyaev et al. (2008) are in agreement with our trend. This suggests that the latitudinal gradient may reverse within a decade, pointing out a complex situation for spatial and temporal variability of SO₂ on various temporal and spatial scales. Large temporal variations of SO₂ and SO were also commonly observed by Sandor et al. (2010), even though their microwave measurements probe at a substantially higher altitude than we do (70–100 km instead of 65–75 km).

4.3.2. Dynamical interpretation of the latitudinal gradient

The past increase in SO₂ from lower to higher latitudes evidenced by Na et al. (1994) and Zasova et al. (1993) could be understood as photochemically driven: SO₂ was more easily photolysed at low latitudes where the UV flux is greater than near the poles. These differences in SO₂ depletion rates are then partially offset by meridional circulation whose influence caused a decrease of these horizontal variations (Yamamoto and Takahashi, 2006). The opposite latitudinal gradient seen recently by Belyaev et al. (2008) and us could then be understood as dynamically driven: at lower latitudes, solar heating activates convection bringing SO₂ from lower altitudes, where it is known to be much more abundant (de Bergh et al., 2006; Bertaux et al., 1996), up to the cloud top level where we can detect it in the UV and where the same UV radiation can photolyze it. Depletion in SO₂ then occurs while advection to higher latitudes by the Hadley cell circulation where the descending branch manifests itself by a positive temperature gradient, a lower altitude of the cloud top and much less SO₂ (Titov et al., 2008; Pätzold et al., 2007). This kind of dynamical explanation is classical and also invoked for OCS and CO in the lower atmosphere of Venus (Marcq et al., 2006) as well for Titan's minor compounds (Vinatier et al., 2010) – but in the opposite direction for both situations. In such a case, a correlation between latitude (or cloud top altitude) and SO₂ mixing ratio should exist. Although we emphasized previously the intrinsic difficulty in translating column densities into mixing ratios, Fig. 17 is showing the same correlation previously shown in Fig. 14 in terms of SO₂ mixing ratios, thus enforcing our dynamical interpretation.

Such a latitudinal pattern can be maintained only while convection at lower latitudes is currently active given the low photo-

chemical lifetime of SO₂, that is while the upper atmosphere is being replenished in SO₂. The VMC/Venus Express camera UV images (at 365 nm) show that at low latitudes, the clouds appear darker than at higher latitudes, and this is interpreted (Titov et al., 2008) as due to convective mixing, bringing ultraviolet absorbers from depth. Clearly, such vertical motions will also bring SO₂ from depth: our measurements of high SO₂ at low latitudes support their hypothesis as well as the possible sudden global SO₂ enrichment event of early 2007 mentioned in the previous section. S. Limaye (private communication) suggested it could be somehow linked to a brightening event at low southern latitudes observed by S. Limaye around orbit #260. If this is the case, a similar enrichment in SO₂ should be noticeable after the major brightening event observed in July 2009 and will be investigated as soon as possible. However, increase in SO₂ mixing ratios should be associated with darkening events such as described in Titov et al. (2008) instead of brightening events if our dynamical interpretation is the right one – actually, a correlation with brightening events would favor the hypothesis of a volcanic origin of SO₂ over our current dynamical explanation.

We therefore found for our 2006–2007 data two main facts: first, there is more SO₂ in the low latitudes regions than in the period covered by Venera 15 (1984–1985), and more than at the end of Pioneer Venus period 1978–1986; second, there is definitely more SO₂ in the low latitude regions than at high latitudes, a situation which is the reverse of Venera-15 data. The decline of SO₂ at low latitudes as observed by Pioneer Venus in 1978–1986 was tentatively interpreted as the result of massive volcanism, just before 1978 (Esposito, 1984). As an alternative to sporadic volcanism, Clancy and Muhleman (1991) suggested that SO₂ variations might be related to changes in the dynamics of Venus mesosphere, a suggestion supported by their (variable) microwave observations of CO, and 5–10 year cyclic variability of cloud top dynamics observed in the UV markings (Pioneer Venus imaging) by del Genio and Rossow (1990). Our SPICAV Fact #1 could be interpreted as well with the two explanations: increase in volcanism, or change in dynamics. But when combined with Fact 2, the dynamical hypothesis is strongly re-enforced w.r.t. the hypothesis of present sporadic volcanism.

5. Conclusion

5.1. Main results

We were able to process SPICAV-UV nadir spectra and to extract spectral radiance factors between 200 and 320 nm with a resolving power $R \sim 200$. We could then compare these radiance factor to synthetic radiance factors computed with a radiative transfer model with various prescribed cloud parametrizations and minor species vertical profiles (SO₂ and SO). Our main findings regarding the visible SO₂ and SO column densities are:

1. SO₂ observable column density decreases with increasing latitude from 5 to 50 $\mu\text{m-atm}$ (with large spatial and temporal variability) at low latitudes to an upper limit of 5 $\mu\text{m-atm}$ in the polar region, in a very close correlation with cloud top altitude derived from simultaneous IR measurements.
2. SO₂ mixing ratio is in agreement with previous determinations, but higher than their average. Such a trend contradicts the long-term SO₂ decrease previously observed in the 1980s and early 1990s.
3. A sudden increase in SO₂ visible column density at all latitudes has occurred since early 2007. The most probable cause would be a convective event enabling some deeper SO₂ content to reach higher, visible layers.

5.2. Future prospects

The difficulties encountered in the modeling of the spectral intervals dominated by aerosols, as well as in the choice of a realistic cloud parametrization points out that significant improvements on our results could be done in a near-future once the spatial variability of the upper clouds and hazes will be better understood. A joint study with the other *Venus Express* instrument sensitive in the UV range, VMC, could be of great interest here – VMC field of view and spatial resolution would complement SPICAV-UV spectroscopic capabilities in a beneficial way. A possible collaboration would consist in investigating possible correlations between gaseous content (SO₂ and SO), radiance at 240 nm where gaseous absorption is minimal with SPICAV and simultaneous reflectivity maps at 365 nm (in the peak absorption of the unknown UV absorber) with VMC. VIRTIS-Visible channel can also be used to fill the spectral data gap between SPICAV-UV and infrared data, especially in the spectral region dominated by the unknown UV absorber near 365 nm region.

Even using solely SPICAV-UV, three phenomena already mentioned should be investigated in closer detail very soon:

- looking for any correlation between some so-called “brightening events” and sudden increases in SO₂ column density;
- confirming the identification of the polar 250-nm absorption feature as O₃, as well as measuring O₃ column density in such as case by adding O₃ to our radiative transfer model;
- investigating upon the origin of the spectral feature near 205 nm.

Acknowledgments

Venus Express is a space mission from the European Space Agency (ESA). We wish to thank all ESA members who participated in this successful mission, and in particular H. Svedhem and O. Witasse. We also thank Astrium for the design and construction of the spacecraft. We thank our collaborators at Service d'Aronomie/France, BIRA/Belgium and IKI/Russia for the design and fabrication of the instrument. We thank CNRS and CNES for funding SPICAV/SOIR in France, the Belgian Federal Science Policy Office, the European Space Agency (ESA, PRODEX program), Roskosmos and the Russian Academy of Sciences. The Russian team acknowledges support from the Russian Foundation for Basic Research, and from the Russian Science Support Foundation. One of us (Denis Belyaev) acknowledges support from CNES for a post-doc position at LATMOS. Anna Fedorova's work is supported by a grant from the Russian Fund of Fundamental Investigations (RFFI, #08-02-01383). We also want to thank E. Lellouch (LESIA) for the improvements suggested during the reviewing process.

References

- Barker, E.S., 1979. Detection of SO₂ in the UV spectrum of Venus. *Geophys. Res. Lett.* 6, 117–120.
- Belyaev, D., Korablev, O., Fedorova, A., Bertaux, J., Vandaele, A., Montmessin, F., Mahieux, A., Wilquet, V., Drummond, R., 2008. First observations of SO₂ above Venus' clouds by means of solar occultation in the infrared. *J. Geophys. Res. (Planets)* 113, 1–10.
- Bertaux, J., Widemann, T., Hauchecorne, A., Moroz, V.I., Ekonomov, A.P., 1996. VEGA 1 and VEGA 2 entry probes: An investigation of local UV absorption (220–400 nm) in the atmosphere of Venus (SO₂, aerosols, cloud structure). *J. Geophys. Res.* 101, 12709–12746.
- Bertaux, J., and 15 colleagues, 2006. SPICAM on Mars Express: Observing modes and overview of UV spectrometer data and scientific results. *J. Geophys. Res. (Planets)* 111, 10–49.
- Bertaux, J.L., and 35 colleagues, 2007. SPICAV on Venus Express: Three spectrometers to study the global structure and composition of the Venus atmosphere. *Planet. Space Sci.* 55, 1673–1700.
- Clancy, R.T., Muhleman, D.O., 1991. Long-term (1979–1990) changes in the thermal, dynamical, and compositional structure of the Venus mesosphere as inferred from microwave spectral line observations of C-120, C-130, and CO-18. *Icarus* 89, 129–146.
- Conway, R.R., McCoy, R.P., Barth, C.A., Lane, A.L., 1979. IUE detection of sulfur dioxide in the atmosphere of Venus. *Geophys. Res. Lett.* 6, 629–631.
- Crutzen, P.J., 2006. Albedo enhancement by stratospheric sulfur injections: A contribution to resolve a policy dilemma? *Climatic Change* 77, 211–220.
- de Bergh, C., Moroz, V.I., Taylor, F.W., Crisp, D., Bézard, B., Zasova, L.V., 2006. The composition of the atmosphere of Venus below 100 km altitude: An overview. *Planet. Space Sci.* 54, 1389–1397.
- del Genio, A.D., Rossow, W.B., 1990. Planetary-scale waves and the cyclic nature of cloud top dynamics on Venus. *J. Atmos. Sci.* 47, 293–318.
- Esposito, L.W., 1984. Sulfur dioxide – Episodic injection shows evidence for active Venus volcanism. *Science* 223, 1072–1074.
- Esposito, L.W., Winick, J.R., Stewart, A.I., 1979. Sulfur dioxide in the Venus atmosphere – Distribution and implications. *Geophys. Res. Lett.* 6, 601–604.
- Esposito, L.W., Copley, M., Eckert, R., Gates, L., Stewart, A.I.F., Worden, H., 1988. Sulfur dioxide at the Venus cloud tops, 1978–1986. *J. Geophys. Res.* 93, 5267–5276.
- Ignatiev, N.I., Titov, D.V., Piccioni, G., Drossart, P., Markiewicz, W.J., Cottini, V., Roatsch, T., Almeida, M., Manoel, N., 2009. Altimetry of the Venus cloud tops from the Venus Express observations. *J. Geophys. Res. (Planets)* 114, 1–10.
- Leblanc, F., Witasse, O., Winningham, J., Brain, D., Liliensten, J., Blély, P., Frahm, R.A., Halekas, J.S., Bertaux, J.L., 2006. Origins of the martian aurora observed by Spectroscopy for Investigation of Characteristics of the Atmosphere of Mars (SPICAM) on board Mars Express. *J. Geophys. Res. (Space Phys.)* 111, 9313–9321.
- Lucy, L.B., 1974. An iterative technique for the rectification of observed distributions. *Astron. J.* 79, 745–754.
- Marcq, E., Encrenaz, T., Bézard, B., Birlan, M., 2006. Remote sensing of Venus' lower atmosphere from ground-based IR spectroscopy: Latitudinal and vertical distribution of minor species. *Planet. Space Sci.* 54, 1360–1370.
- Markwardt, C.B., 2009. Non-linear least-squares fitting in IDL with MPFIT. In: Bohlender, D.A., Durand, D., Dowler, P. (Eds.), *Astronomical Society of the Pacific Conference Series*, pp. 251–254.
- McClintock, W.E., Barth, C.A., Kohnert, R.A., 1994. Sulfur dioxide in the atmosphere of Venus. 1: Sounding rocket observations. *Icarus* 112, 382–388.
- Mills, F.P., Allen, M., 2007. A review of selected issues concerning the chemistry in Venus' middle atmosphere. *Planet. Space Sci.* 55, 1729–1740.
- Moroz, V.I., Zasova, L.V., 1997. VIRA-2: A review of inputs for updating the Venus international reference atmosphere. *Adv. Space Res.* 19, 1191–1201.
- Na, C.Y., Esposito, L.W., Skinner, T.E., 1990. International ultraviolet explorer observations of Venus SO₂ and SO. *J. Geophys. Res.* 95, 7485–7491.
- Na, C.Y., Esposito, L.W., McClintock, W.E., Barth, C.A., 1994. Sulfur dioxide in the atmosphere of Venus. 2: Modeling results. *Icarus* 112, 389–395.
- Pariset, J.P., Rigaud, P., Hugué, D., 1986. Balloon observations of Venus from 200 to 320 nm. *Astron. Astrophys.* 166, 333–336.
- Parkinson, W., 2003. Absolute absorption cross section measurements of CO₂ in the wavelength region 163–200 nm and the temperature dependence. *Chem. Phys.* 290, 251–256.
- Pätzold, M., and 10 colleagues, 2007. The structure of Venus' middle atmosphere and ionosphere. *Nature* 450, 657–660.
- Phillips, L.F., 1981. Absolute absorption cross sections for SO between 190 and 235 nm. *J. Phys. Chem.* 85, 3994–4000.
- Rufus, J., Stark, G., Smith, P.L., Pickering, J.C., Thorne, A.P., 2003. High-resolution photoabsorption cross section measurements of SO₂, 2: 220 to 325 nm at 295 K. *J. Geophys. Res. (Planets)* 108, 5011–5016.
- Sandor, B.J., Todd Clancy, R., Moriarty-Schieven, G., Mills, F.P., 2010. Sulfur chemistry in the Venus mesosphere from SO₂ and SO microwave spectra. *Icarus* 208, 49–60.
- Sneep, M., Ubachs, W., 2005. Direct measurement of the Rayleigh scattering cross section in various gases. *J. Quant. Spectrosc. Radiat. Trans.* 92, 293–310.
- Stamnes, K., Tsay, S., Jayaweera, K., Wiscombe, W., 1988. Numerically stable algorithm for discrete-ordinate-method radiative transfer in multiple scattering and emitting layered media. *Appl. Opt.* 27, 2502–2509.
- Stewart, A.I., Anderson, D.E., Esposito, L.W., Barth, C.A., 1979. Ultraviolet spectroscopy of Venus – Initial results from the Pioneer Venus orbiter. *Science* 203, 777–779.
- Thuillier, G., and 11 colleagues, 2009. SOLAR/SOLSPEC: Scientific objectives, instrument performance and its absolute calibration using a blackbody as primary standard source. *Sol. Phys.* 257, 185–213.
- Titov, D.V., Taylor, F.W., Svedhem, H., Ignatiev, N.I., Markiewicz, W.J., Piccioni, G., Drossart, P., 2008. Atmospheric structure and dynamics as the cause of ultraviolet markings in the clouds of Venus. *Nature* 456, 620–623.
- Villard, E., 2008. L'instrument SPICAV d'étude de l'atmosphère de Vénus sur la mission Venus Express : caractérisation instrumentale et observations en vol. Ph.D. Thesis, Université de Versailles St-Quentin-en-Yvelines.
- Vinatier, S., and 10 colleagues, 2010. Analysis of Cassini/CIRS limb spectra of Titan acquired during the nominal mission. I. Hydrocarbons, nitriles and CO₂ vertical mixing ratio profiles. *Icarus* 205, 559–570.
- Wallace, L., Caldwell, J.J., Savage, B.D., 1972. Ultraviolet photometry from the orbiting astronomical observatory. III. Observations of Venus, Mars, Jupiter, and Saturn longward of 2000 Å. *Astrophys. J.* 172, 755–769.
- Wiscombe, W., 1977. The delta-M method: Rapid yet accurate radiative flux calculations for strongly asymmetric phase functions. *J. Atmos. Sci.* 36, 1408–1422.

- Wu, R.C.Y., Yang, B.W., Chen, F.Z., Judge, D.L., Caldwell, J., Trafton, L.M., 2000. Measurements of high-, room-, and low-temperature photoabsorption cross sections of SO₂ in the 2080- to 2950-Å region, with application to Io. *Icarus* 145, 289–296.
- Yamamoto, M., Takahashi, M., 2006. An aerosol transport model based on a two-moment microphysical parameterization in the Venus middle atmosphere: Model description and preliminary experiments. *J. Geophys. Res. (Planets)* 111, 8002–8013.
- Zasova, L.V., Moroz, V.I., Esposito, L.W., Na, C.Y., 1993. SO₂ in the middle atmosphere of Venus: IR measurements from Venera-15 and comparison to UV data. *Icarus* 105, 92–109.